LETTER

Classical shear cracks drive the onset of dry frictional motion

Ilya Svetlizky[1] & Jay Fineberg[1]

Frictional processes entail the rupture[1,2] of the ensemble of discrete contacts defining a frictional interface[3,4]. There are a variety of views on how best to describe the onset of dry frictional motion. These range from modelling friction with a single degree of freedom, a 'friction coefficient'[3,5], to theoretical treatments using dynamic fracture[5–8] to account for spatial and temporal dynamics along the interface. We investigated the onset of dry frictional motion by performing simultaneous high-speed measurements of the real contact area and the strain fields in the region surrounding propagating rupture tips within the dry (nominally flat) rough interfaces formed by brittle polymer blocks. Here we show that the transition from 'static' to 'dynamic' friction is quantitatively described by classical singular solutions for the motion of a rapid shear crack[5,9–13]. We find that these singular solutions, originally derived to describe brittle fracture, are in excellent agreement with the experiments for slow propagation, whereas some significant discrepancies arise as the rupture velocity approaches the Rayleigh wave speed. In addition, the energy dissipated in the fracture of the contacts remains nearly constant throughout the entire range in which the rupture velocity is less than the Rayleigh wave speed, whereas the size of the dissipative zone undergoes a Lorentz-like contraction as the rupture velocity approaches the Rayleigh wave speed. This coupling between friction and fracture is critical to our fundamental understanding of frictional motion and related processes, such as earthquake dynamics.

A dry frictional interface is composed of an ensemble of discrete contacts whose total area (the real contact area, A) is orders of magnitude smaller than the nominal contact area[4]. Local motion (slip) is initiated when contacts are broken via propagating ruptures[1]. Characterization of the dynamic fields that drive these ruptures and how they couple to the dissipative mechanisms on the interface are therefore critical to our fundamental understanding of frictional motion. These fields also describe the elastic radiation emitted by the rupture whose form is important to interpretation of near-field seismic signals radiated by earthquakes[14,15].

Linear elastic fracture mechanics[10] (LEFM) is the fundamental theoretical framework describing brittle fracture. LEFM predicts a universal singular form of stresses (and strains) in the vicinity of a crack tip. These singular stresses are only regularized by dissipative[10–13] processes that take place as this singular limit is approached. Shear-driven (mode II) fracture is generally considered to be impossible in bulk isotropic materials[9] because it is believed that a crack will rotate under imposed shear so as to fracture under pure tension. An exception to this may occur for highly anisotropic conditions, as in the case of the weak interface plane that defines a frictional interface[11,16–18]. Examples of such systems range from natural faults to single adhesive contacts. Although both contact separation[8] and earthquake dynamics[5,7,12,13,15] have long been theoretically described using fracture mechanics, there has been no direct experimental evidence that quantitative predictions of LEFM, such as the universal singular forms of stresses and material motion at tips of rapidly moving ruptures, really occur in frictional failure. We will demonstrate that, in the brittle material studied, frictional ruptures along dry and (nominally flat) rough interfaces can indeed be quantitatively described by LEFM.

We study the structure of the elastic fields driving ruptures that propagate within an interface formed between two initially flat poly(methylmethacrylate) blocks, which were uniformly roughened to a 3-μm r.m.s. roughness. The blocks are pressed together with an externally imposed normal force, $F_N = 5,500$ N (5 MPa of nominal pressure). Once F_N is applied, a shear force, F_S, is quasi-statically incremented until stick-slip motion initiates (Fig. 1a). The complete two-dimensional strain tensor, $\varepsilon_{ij}(t)$, is measured at 19 locations along and $\sim$3.5 mm above the interface at 1,000,000 samples per second (Fig. 1a). We simultaneously measure the displacement parallel to the interface, u_x, at specific locations adjacent to the strain gages. At the same time, we measure the real contact area, $A(x,t)$, with high spatial resolution at 580,000 frames per second (see Methods). We focus on the short time intervals bracketing slip initiation.
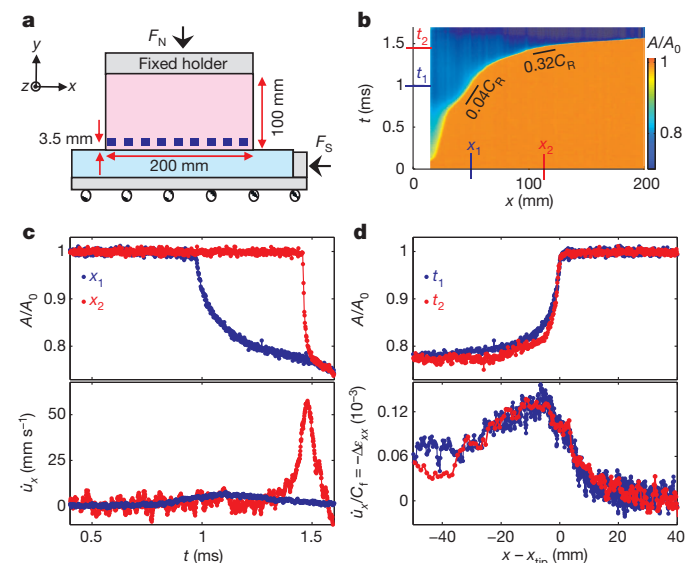

Figure 1 | Experimental system and slow rupture scaling. a, 19 Rosette strain gauges (blue squares) are mounted 3.5 mm above the frictional interface. The three strain components were measured simultaneously every 1 μs. **b**, The evolution of real contact area, $A(x,t)$ (normalized at nucleation time, $t = 0$), along the 200-mm quasi-one-dimensional interface of a slow rupture front, which nucleated at $x = 0$ and accelerated to $0.3C_R$. **c**, $A(t)$ (top) and $\dot{u}_x(t)$ (bottom) (u_x is the x component of the displacement field measured 3.5 mm above the interface) at locations x_1 (blue dots) and x_2 (red dots) denoted in **b**. **d**, Collapse of both $A(x,t)$ (top) and $\dot{u}_x/C_f$ (bottom) is obtained by plotting the data as a function of the distance $x - x_{tip}$ when the rupture tip, x_{tip}, arrives at x_1 (blue, at time t_1) and x_2 (red, at time t_2). C_f is the local front velocity. $A(x,t_i)$ was measured directly whereas the spatially dependent $\dot{u}_x(x)$ was constructed from the time series $\dot{u}_x(t)$ using $\dot{u}_x(x,t) = \dot{u}_x(x - C_f t)$. Variations of $C_f(x)$ are accounted for as described in Methods. During the front's passage, $-\dot{u}_x/C_f$ corresponds to changes of the strain component parallel to the interface, $\Delta\varepsilon_{xx}$.

[1]The Racah Institute of Physics, The Hebrew University of Jerusalem, Givat Ram, Jerusalem 91904, Israel.

We define the location of a rupture front, x_{tip}, as the point where the initial value of $A(x,t)$ is reduced by 3%. x_{tip} both represents the fracture of contacts and signals the initiation of local slip[2]. For a steadily moving front, $\varepsilon_{ij}(x,t) = \varepsilon_{ij}(x - C_f t)$, where C_f is the rupture front velocity. When C_f varies slowly, $\varepsilon_{ij}(x,t) = \varepsilon_{ij}(x - \int C_f dt)$, enabling conversion from temporal $\varepsilon_{ij}(t)$ to spatial measurements $\varepsilon_{ij}(x - x_{tip})$, using $C_f(t)$ obtained from $A(x,t)$ measurements (see Methods). For each front passage we define strain tensor variations, $\Delta\varepsilon_{ij}$, by subtracting the initial strains from ε_{xx} and ε_{yy} and residual strain from ε_{xy}.

We present a typical measurement of $A(x,t)$ for a slow, but accelerating, rupture front in Fig. 1b. C_f is well below the Rayleigh wave speed, C_R ($\sim$1,255 m s^{-1}) over the entire duration of this experiment. As C_f increases, the timescale of the weakening process (drop of $A(x,t)$) shortens (Fig. 1c, top) and material element velocities, $\dot{u}_x$ (u is the displacement field), increase significantly (Fig. 1c, bottom). In contrast to $A(x,t)$, which is an interfacial property, $\dot{u}_x$ constitutes a lower bound of the slip velocity at the interface, because it is measured 3.5 mm from the interface (see Methods). When plotted in the reference frame of the moving rupture tip, $x - x_{tip}$, the $A(x,t)$ collapse (Fig. 1d, top) to a single curve. Furthermore, $\dot{u}_x(x)$, when scaled by C_f, collapses to a well-defined functional form (Fig. 1d, bottom) corresponding to $\Delta\varepsilon_{xx} = -\dot{u}_x(x)/C_f$ (Extended Data Fig. 2). Note that contacts are broken for $x - x_{tip} < 0$ and unbroken when $x - x_{tip} > 0$.

Figure 2a demonstrates that for slow ruptures ($\sim$0.01$C_R < C_f < \sim$0.3C_R) the measured variations of each strain tensor component, $\Delta\varepsilon_{ij}$, collapse to well-defined functional forms. This breaks down as C_f increases; all $\Delta\varepsilon_{ij}$ amplitudes grow significantly while strain oscillations

are strongly amplified. Typical measurements of $\Delta\varepsilon_{ij}$ for high velocities (0.96C_R) are presented in Fig. 2b.

We now compare the measured strains, ε_{ij}, to the universal asymptotic solutions for mode II cracks predicted by LEFM. In our experiment, external tensile stresses ($\sigma^0_{xx}, \sigma^0_{yy}$) exist and the crack faces are subjected to a residual frictional shear stress, τ^r, so that the stresses can be written as $\sigma_{ij} = \Delta\sigma_{ij} + \begin{pmatrix} \sigma^0_{xx} & \tau^r \\ \tau^r & \sigma^0_{yy} \end{pmatrix}$. Owing to the linearity of the governing equations, the stress field variations, $\Delta\sigma_{ij}$, can be mapped[11] to the stress-free conditions that define the mode II crack problem. Therefore, near the rupture tip, $\Delta\sigma_{ij}$ have the singular form:

$$\Delta\sigma_{ij} = \frac{K_{II}}{\sqrt{2\pi r}} \Sigma^{II}_{ij}(\theta, C_f) \qquad (1)$$

where (r, θ) are polar coordinates relative to the crack tip, $\Sigma^{II}_{ij}(\theta, C_f)$ is a known universal function and K_{II} is a scalar coefficient known as the stress intensity factor[10]. $\Delta\sigma_{ij}$ are linearly related to the measured strain variations $\Delta\varepsilon_{ij}$ via the elastic moduli and the use of plane strain boundary conditions (see Methods). Because the strain gauges are displaced from the interface, each $\Delta\varepsilon_{ij}(x)$ measurement involves both radial (50 mm > r > 3.5 mm) and angular (0 < θ < π) variations (see Fig. 2c).

In Fig. 2a we show that for slow ruptures all of the measured strain components $\Delta\varepsilon_{ij}$ agree well with the strains corresponding to equation (1) (black lines), where the only free parameter is K_{II}. The apparent data collapse in Fig. 2a occurs because these LEFM solutions for $C_f < 0.4C_R$ are indistinguishable. K_{II} is related to G, the energy flux per unit area (the energy release rate), via[10]:

$$G = \frac{(1 - v^2)}{E} f_{II}(C_f) K^2_{II} \qquad (2)$$

where $f_{II}(C_f)$ is a known universal function that is fairly constant for low velocities and diverges as $C_f \rightarrow C_R$. When G is balanced by the fracture energy Γ (the energy dissipated per unit area), equation (2) uniquely relates K_{II} for each C_f to Γ. Using equation (1) to measure K_{II}, the energy balance condition ($G = \Gamma$) therefore yields a single value $\Gamma \approx 1.1 \pm 0.3$ J m^{-2} for the LEFM predictions presented in Fig. 2a over 0.01$C_R < C_f < \sim$0.3C_R.

A typical example of rupture at high C_f (Fig. 2b) demonstrates that for the same constant value of Γ most characteristic features of $\Delta\varepsilon_{ij}$ observed at higher rupture velocities are also well described by equation (1). For example, the violent high-amplitude strain oscillations that occur when the rupture tip passes beneath the measurement point (Fig. 2c) are due to the singular nature of $\Sigma^{II}_{ij}(\theta, C_f)$. Figure 2b, top, however, demonstrates that equation (1) clearly fails to describe $\Delta\varepsilon_{xy}$ for $x - x_{tip} > 0$.

To systematically study how $\Delta\varepsilon_{ij}$ varies over 0.01 < C_f < 0.99C_R, we characterize $\Delta\varepsilon_{ij}$ variations using $\delta\varepsilon_{xx}, \delta\varepsilon_{yy}, \delta\varepsilon_{xy}$ and $\delta\varepsilon^{Osc}_{xy}$, as defined in the insets within Fig. 3. With the only input being the constant value of Γ measured at low velocities, we see that, for all C_f, the theory quantitatively describes both the strain variations $\delta\varepsilon_{xx}$ and $\delta\varepsilon_{yy}$ (Fig. 3a) and the violent high-amplitude strain oscillations, $\delta\varepsilon^{Osc}_{xy}$, (Fig. 3b, top) evident in the example in Fig. 2b.

Although $\delta\varepsilon_{xy}$ is also well-described by the theory for $C_f/C_R < 0.4$, we find (Fig. 3b, bottom) that a systematic failure of the classic universal form predicted by LEFM (equation (1)) occurs, as seen in Fig. 2b, top. These deviations are first observed at $C_f \approx 0.7C_R$ and increase dramatically as $C_f \rightarrow C_R$; experiments reveal a sharp and systematic increase of $\delta\varepsilon_{xy}$, whereas the theory predicts vanishingly small values as $C_f \rightarrow C_R$. Note that for $C_f/C_R < 0.4$ the apparent collapse of all strain components (Fig. 2a) is a natural consequence of the theory.

We now consider the value of Γ. Whereas the bulk fracture energy, $\Gamma_{bulk} = 2,000$ J m^{-2}, is a material property of poly(methylmethacrylate), the interface value, Γ, is directly related to $A(x,t)$, which is determined by F_N. It is interesting that the measured value $\Gamma = 1.1$ J m^{-2} for our experimental conditions is approximately Γ_{bulk} when the sparseness of the contacts[4] ($A \ll A_{nominal}$) is accounted for (see Methods).
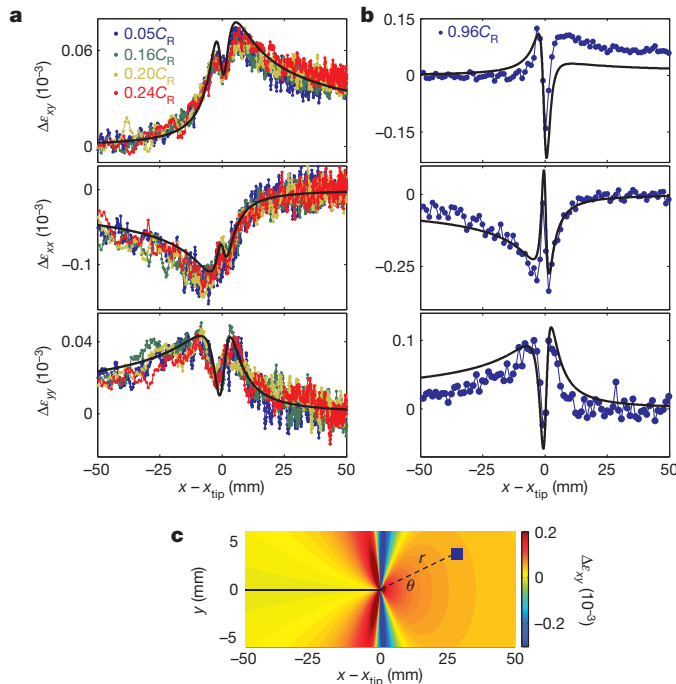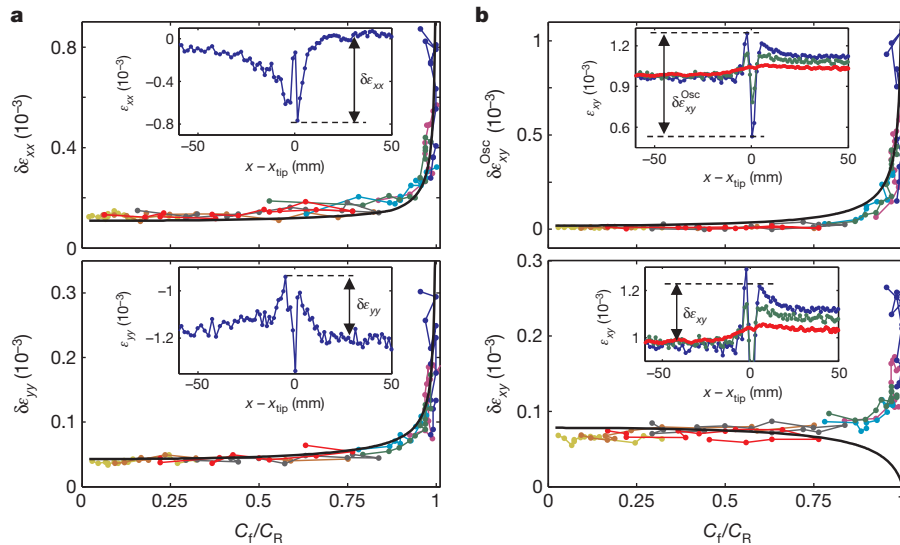

Figure 2 | The functional form of the elastic strains. a, Measurements of strain tensor variations, $\Delta\varepsilon_{ij}$, after subtracting the initial strain from ε_{xx} and ε_{yy} and residual strain from ε_{xy}. Colours represent different slow front velocities (0.05$C_R < C_f < 0.24C_R$; see key). Corresponding LEFM predictions (equation (1)) for plane strain boundary conditions are plotted in black ($C_f = 0.2C_R$). The fracture energy $\Gamma \approx 1.1$ J m^{-2} is the sole free parameter. **b**, The mean value of $\Delta\varepsilon_{ij}$ for three typical measurements at $C_f \approx 0.96C_R$. Equation (1) is plotted (black line) for the same Γ as in **a**, and still describes the larger amplitudes and strong oscillations of rapidly propagating ruptures. **c**, Shear strain variations, $\Delta\varepsilon_{xy}$, surrounding the rupture tip predicted by equation (1) for $C_f = 0.96C_R$. The blue square denotes the strain gauge location relative to the approaching rupture tip. Note the strong angular dependence that drives the violent oscillations in **b**.

Figure 3 | Systematic comparison of measured strains to LEFM.
a, Measured elastic strains, ε_{xx} (top, inset) and ε_{yy} (bottom, inset), are characterized by their signal amplitudes, $\delta\varepsilon_{xx}$ and $\delta\varepsilon_{yy}$ (black arrows). Main panels: $\delta\varepsilon_{xx}$ (top) and $\delta\varepsilon_{yy}$ (bottom) are plotted for $0.01C_R < C_f < 0.99C_R$. **b**, We characterize ε_{xy} by the oscillatory amplitude, $\delta\varepsilon_{xy}^{Osc}$ (top, inset) and the shear strain drop, $\delta\varepsilon_{xy}$ (bottom, inset). **a, b**, $C_R = 1{,}255 \pm 10\,\mathrm{m\,s^{-1}}$, plotted

strains are in units of 10^{-3}. Colours represent different stick-slip sequences, where different measurement locations are connected by a solid line. Classic LEFM predictions, for constant $\Gamma \approx 1.1\,\mathrm{J\,m^{-2}}$, are plotted in black. Equation (1) successfully describes $\delta\varepsilon_{xx}$, $\delta\varepsilon_{yy}$ (**a**) and $\delta\varepsilon_{xy}^{Osc}$ (**b**, top) while systematically failing to describe $\delta\varepsilon_{xy}$ (**b**, bottom).

This suggests that significant plastic deformation (the major contribution to Γ_{bulk}) may also take place within the contacting asperities, as surmised in ref. 2.

Although LEFM enables us to measure Γ, it does not address the details of the dissipative region. As $A(x,t)$ is measured on the interface, it characterizes cohesive zone (interface weakening region) properties. Figure 4a reveals that the contact area reduction, ΔA, increases with C_f, suggesting that corrections to our assumption of constant Γ may be required at high velocities. Γ could indeed vary significantly in the singular ($C_f \approx C_R$) region of $\Delta\varepsilon_{ij}$ while still being consistent with the data, as when approaching the singularity our finite ($\pm 10\,\mathrm{m\,s^{-1}}$) measurement accuracy of C_f and C_R limits our ability to resolve Γ.

Although the non-monotonic behaviour of A with $x - x_{tip}$ suggests interesting dynamics as $C_f \to C_R$, for reasons of simplicity we characterize the scale over which $A(x,t)$ is reduced by single length scale, X_c (Fig. 4a, bottom). We suggest that X_c provides a direct measure of the cohesive zone size. Figure 4b demonstrates that X_c is not constant, but systematically contracts with increasing C_f. As $C_f \to C_R$, X_c appears to

Figure 4 | 'Lorentz' contraction of the cohesive zone. a, Top; the contact area reduction, A/A_0, increases for faster ruptures and non-monotonic behaviour is observed for $C_f > 0.9C_R$. Bottom, we characterize the weakening region (the reduction of A) by X_c, the length scale where a 60% reduction of $\Delta A/A_0$ occurs. Contraction of X_c with C_f is apparent. **b**, X_c as a function of C_f. Colours represent the different slip events in Fig. 3. Black line: LEFM prediction, $X_c = X_c^0/f_{II}(C_f)$, where $X_c^0 = X_c(C_f \approx 0)$. $X_c(C_f \approx C_R) < 0.5\,\mathrm{mm}$ are limited by our temporal resolution.

approach zero. Fracture mechanics predicts such an effective 'Lorentz' contraction of all length scales in the propagation direction[5,10,12]. In particular, we expect $X_c = X_c^0/f_{II}(C_f)$, where $f_{II}(C_f)$ is the universal function (equation (2)) relating K_{II} to G, which diverges at C_R and $X_c^0 = X_c(C_f = 0)$. Figure 4b (black line) demonstrates that this general result of elastodynamic theory describes the measurements well.

Figure 4b indicates that in the slow rupture regime, strain measurements were performed at scales of $\sim X_c$, which characterizes the scale of the cohesive zone. The universal form, predicted by equation (1), is expected to describe the elastic fields at distances far from the cohesive zone, but still small compared to other dimensions of the system[11]. The good agreement with LEFM (Fig. 2a) is, nevertheless, consistent (see Extended Data Fig. 4) with simple cohesive zone models coupled to LEFM[11].

In this light, as X_c contracts by nearly an order of magnitude as $C_f \to C_R$, we should expect equation (1) to become increasingly more accurate in precisely the velocity regime where it performs badly (compare $\delta\varepsilon_{xy}$ in Fig. 3b, bottom). $\delta\varepsilon_{xy}(C_f)$, as Fig. 3b, inset, demonstrates, correlates with the initially imposed shear stresses ahead of the front. These initial stresses have been shown to govern rupture velocity selection[19–21]. Higher order contributions to this LEFM solution (see Extended Data Fig. 5) do not correct these discrepancies. As ruptures where $C_f \to C_R$ are commonplace in both frictional failure and earthquake dynamics, understanding this failure of the classical LEFM solution is important; the form of the singular stress fields surrounding rapid ruptures has significant ramifications for earthquake branching and fault bifurcation[22].

Knowledge of Γ and X_c enables us to estimate elusive but long-sought[13,16–18] dynamical quantities at the interface that include peak stresses and slip velocities. The contraction of X_c tells us (see Methods) that quantities measured off-interface increasingly deviate from their interface values as $C_f \to C_R$; for example, the peak value (strain $= 0.8 \times 10^{-3}$) of $\delta\varepsilon_{xx}$ ($= -\dot{u}_x/C_f$), which corresponds to $\dot{u}_x \approx 1\,\mathrm{m\,s^{-1}}$, can be an order of magnitude higher on the interface[18].

Whereas we have demonstrated that equations (1) and (2) provide an excellent description of the fields that drive frictional motion in a specific material under dry conditions, we expect the results to be generally valid as long as the assumptions underpinning the LEFM solution are obeyed. These are: (1) the dissipative scale is small compared to the size of the elastic region in which the stress singularity
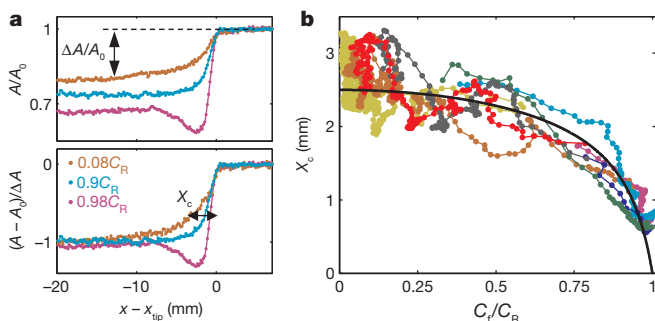
develops; and (2) the residual stress, τ^r, remains fairly constant. So long as the dissipative region is sufficiently confined, its precise nature (for example, whether granular, powdered or consisting of contacting asperities) only contributes to the value of $\Gamma(C_f)$. This description may have to be adapted for lubricated boundaries where τ^r may be strongly slip-rate dependent[6], or even break down within highly damaged regions whose spatial extent is large compared to the surrounding elastic material.

The measurements in Figs 2 and 3 may therefore provide a precise quantitative framework for describing frictional motion along rough, nominally flat, surfaces. Such high-speed strain measurements[14] are rarely performed adjacent to natural faults. It is interesting to consider if the universal description of strains observed here is also valid during earthquakes. If so, high-speed single-point measurements of $\Delta \varepsilon_{ij}$ adjacent to faults could provide sensitive measurements of both earthquake velocities and Γ. These measurements could reveal rupture-velocity dependence of both intrinsic values of Γ and values resulting from near-fault damage. These measurements could also clearly differentiate between different types of fracture modes such as supershear[15] or slow ruptures, which are increasingly observed in both experiments[1,23–25] and natural faults[26]. Our results indicate that the structure of slow ruptures is characterized by LEFM. The mechanisms governing their appearance are, however, not yet clear and may depend on properties of the underlying friction law (for example, a velocity strengthening range)[27,28].

Let us now consider the threshold for frictional failure. Recent studies[14,29,30] have shown that the static friction coefficient is not a material property, but depends on the applied loading. The failure of bulk materials is described by the Griffith condition—the critical energy release rate, G_{crit}, being equal to Γ. We have shown that interface rupture propagation is described by, essentially, the same framework. This suggests that an analogous 'Griffith' condition may exist for the onset of rupture propagation for a frictional interface, and by incorporating applied loading conditions it may be possible to calculate G_{crit}.

METHODS SUMMARY

The Methods section contains additional material about sample preparation and characterization together with detailed descriptions of the loading system, real contact area measurements, slip and strain measurements. Also presented is a comparison between direct measurements of the material velocities and derived values obtained using the relation $\delta \varepsilon_{xx} = -\dot{u}_x/C_f$. More detailed descriptions of the analysis techniques (comparison of LEFM to measured strains, converting temporal to spatial measurements) used in the manuscript are also presented. Included is additional information that demonstrates that both higher-order (non-singular) strain field terms and the existence of a (simple) cohesive zone of size X_c have negligible effects on the comparisons of equation (1) to the data measured in our experiments. We additionally include a brief section that shows how estimates of cohesive zone properties (peak stress, interface slip velocity, and weakening distance on the interface) can be obtained from our measurements of Γ and X_c. We also describe how we relate the measured value of Γ to measured bulk values, Γ_{bulk}, of the fracture energy.

1. Rubinstein, S. M., Cohen, G. & Fineberg, J. Detachment fronts and the onset of dynamic friction. *Nature* **430,** 1005–1009 (2004).
2. Ben-David, O., Rubinstein, S. M. & Fineberg, J. Slip-stick and the evolution of frictional strength. *Nature* **463,** 76–79 (2010).
3. Bowden, F. P. & Tabor, D. *The Friction and Lubrication of Solids* 2nd edn (Oxford Univ. Press, 2001).
4. Dieterich, J. H. & Kilgore, B. D. Imaging surface contacts: power law contact distributions and contact stresses in quartz, calcite, glass and acrylic plastic. *Tectonophysics* **256,** 219–239 (1996).
5. Scholz, C. H. *The Mechanics of Earthquakes and Faulting* 2nd edn (Cambridge Univ. Press, 2002).
6. Brener, E. A. & Marchenko, V. I. Frictional shear cracks. *JETP Lett.* **76,** 211–214 (2002).
7. Ben-Zion, Y. Collective behavior of earthquakes and faults: continuum-discrete transitions, progressive evolutionary changes, and different dynamic regimes. *Rev. Geophys.* **46,** RG4006 (2008).
8. Johnson, K. L. Adhesion and friction between a smooth elastic spherical asperity and a plane surface. *Proc. R. Soc. Lond. A* **453,** 163–179 (1997).
9. Fineberg, J. & Marder, M. Instability in dynamic fracture. *Phys. Rep.* **313,** 1–108 (1999).
10. Freund, L. B. *Dynamic Fracture Mechanics* (Cambridge, 1990).
11. Palmer, A. C. & Rice, J. R. The growth of slip surfaces in the progressive failure of over-consolidated clay. *Proc. R. Soc. Lond. A* **332,** 527–548 (1973).
12. Rice, J. R. in *Physics of the Earth's Interior* (eds Dziewonski, A. M. & Boschi, E.) 555–649 (Italian Physical Society and North-Holland, 1980).
13. Ida, Y. Cohesive force across tip of a longitudinal-shear crack and Griffiths specific surface energy. *J. Geophys. Res.* **77,** 3796–3805 (1972).
14. Borcherdt, R. D., Johnston, M. J. S., Glassmoyer, G. & Dietel, C. Recordings of the 2004 Parkfield earthquake on the General Earthquake Observation System array: implications for earthquake precursors, fault rupture, and coseismic strain changes. *Bull. Seismol. Soc. Am.* **96,** S73–S89 (2006).
15. Dunham, E. M. & Archuleta, R. J. Evidence for a supershear transient during the 2002 Denali fault earthquake. *Bull. Seismol. Soc. Am.* **94,** S256–S268 (2004).
16. Okubo, P. G. & Dieterich, J. H. Effects of physical fault properties on frictional instabilities produced on simulated faults. *J. Geophys. Res.* **89,** 5817–5827 (1984).
17. Ohnaka, M. *The Physics of Rock Failure and Earthquakes* (Cambridge Univ. Press, 2013).
18. Lykotrafitis, G., Rosakis, A. J. & Ravichandran, G. Self-healing pulse-like shear ruptures in the laboratory. *Science* **313,** 1765–1768 (2006).
19. Ben-David, O., Cohen, G. & Fineberg, J. The dynamics of the onset of frictional slip. *Science* **330,** 211–214 (2010).
20. Trømborg, J., Scheibert, J., Amundsen, D. S., Thøgersen, K. & Malthe-Sørenssen, A. Transition from static to kinetic friction: insights from a 2D model. *Phys. Rev. Lett.* **107,** 074301 (2011).
21. Kammer, D. S., Yastrebov, V. A., Spijker, P. & Molinari, J. F. On the propagation of slip fronts at frictional interfaces. *Tribol. Lett.* **48,** 27–32 (2012).
22. Poliakov, A. N. B., Dmowska, R. & Rice, J. R. Dynamic shear rupture interactions with fault bends and off-axis secondary faulting. *J. Geophys. Res.* **107**(B11), 2295 (2002).
23. Nielsen, S., Taddeucci, J. & Vinciguerra, S. Experimental observation of stick-slip instability fronts. *Geophys. J. Int.* **180,** 697–702 (2010).
24. Latour, S. *et al.* Ultrafast ultrasonic imaging of dynamic sliding friction in soft solids: the slow slip and the super-shear regimes. *Europhys. Lett.* **96,** 59003 (2011).
25. Yamaguchi, T. *et al.* Gutenberg-Richter's law in sliding friction of gels. *J. Geophys. Res.* **116,** B12306 (2011).
26. Beroza, G. C. & Ide, S. Slow earthquakes and nonvolcanic tremor. *Annu. Rev. Earth Planet. Sci.* **39,** 271–296 (2011).
27. Bar Sinai, Y., Brener, E. A. & Bouchbinder, E. Slow rupture of frictional interfaces. *Geophys. Res. Lett.* **39,** L03308 (2012).
28. Kaproth, B. M. & Marone, C. Slow earthquakes, preseismic velocity changes, and the origin of slow frictional stick-slip. *Science* **341,** 1229–1232 (2013).
29. Passelègue, F. X., Schubnel, A., Nielsen, S., Bhat, H. S. & Madariaga, R. From sub-Rayleigh to supershear ruptures during stick-slip experiments on crustal rocks. *Science* **340,** 1208–1211 (2013).
30. Ben-David, O. & Fineberg, J. Static friction coefficient is not a material constant. *Phys. Rev. Lett.* **106,** 254301 (2011).

Author Contributions I.S. performed the measurements. Both authors contributed to the analysis and writing the manuscript.

Author Information Reprints and permissions information is available at www.nature.com/reprints. The authors declare no competing financial interests. Readers are welcome to comment on the online version of the paper. Correspondence and requests for materials should be addressed to J.F. (jay@mail.huji.ac.il).

METHODS

Sample construction. Our experiments were conducted using poly(methylmethacrylate) (PMMA) blocks of dimensions $200\,\text{mm} \times 100\,\text{mm} \times 5.5\,\text{mm}$ (top block) and $290\,\text{mm} \times 28\,\text{mm} \times 30\,\text{mm}$ (bottom block) in the x, y and z direction, respectively (see Fig. 1a). Material shear, C_S, and longitudinal, C_L, wave speeds were obtained by measuring the time of flight of ultrasonic pulses, yielding $C_S = 1{,}345 \pm 10\,\text{m s}^{-1}$ and $C_L = 2{,}700 \pm 10\,\text{m s}^{-1}$. These provide $C_R = 1{,}255 \pm 10\,\text{m s}^{-1}$, where C_R is the Rayleigh wave speed. The values yield dynamic values for the Poisson ratio of $v \approx 1/3$ and Young's modulus of $E = 5.65\,\text{GPa}$. Note the value of E is significantly different from the static value of $E = 3\,\text{GPa}$. This difference is due to the viscoelastic behaviour of PMMA[31]. The contact face of the top block was diamond-machined to optical flatness. The bottom block's contact face was carefully polished first by 15-μm and later by smoother 9-μm diamond standard lapping film, yielding a 3-μm r.m.s. surface roughness.

Loading system. While the loading system was slightly modified and fitted for the purposes of the current research, the experimental system is described in detail elsewhere[19,30]. The top block is clamped at its top edge, while the bottom block is mounted on a low-friction linear translational stage (Fig. 1a). External normal load, F_N, was fixed at the beginning of an experiment by pressing the blocks together in the y direction. Subsequently, external shear force, F_S, was quasi-statically ($40\,\text{N s}^{-1}$) applied (starting from $F_S = 0$) to the bottom block in the negative x direction via a load cell of stiffness $10^7\,\text{N m}^{-1}$. Generally, this procedure results in an induced torque and consequently, strong gradients of normal stresses at the interface (see figure 1 in refs 19, 30). To partially compensate for this effect we varied the loading conditions by slightly tilting the top block before applying F_N.

Real contact area measurements. Changes in the real contact area along the entire interface were measured by an optical method based on total internal reflection. Basic principles are presented in detail elsewhere[32,33]. A sheet of light, incident on the frictional interface at an angle well beyond the critical angle for total internal reflection, is reflected everywhere except at contact points (Extended Data Fig. 1a). This yields an instantaneous transmitted light intensity proportional to A over the entire ($x \times z$) $200 \times 5.5\,\text{mm}$ interface. The transmitted light is continuously imaged (at a spatial resolution of $1{,}280 \times 8$ pixels) at 580,000 frames per second using a high speed camera, Phantom v710. Data acquisition is continuous. The data are temporarily stored in a circular buffer large enough to acquire 7 ms of data both before and after each event. Storage of the data for each dynamic slip event is triggered by a sensitive acoustic sensor that is coupled to the top plate of the system.

The frictional interface is quasi-1D, as its width (z direction), 5.5 mm, is much smaller than any other dimensions of the block. The simultaneous measurements of $A(x,t)$ along the entire 1D interface is obtained by integration of the acquired images over the 8 pixels in the z direction.

We use a high power LED (CBT-90) as our source of light. This is in contrast to refs 32 and 33, where a laser sheet was used. One main advantage of a noncoherent light source is the absence of interference patterns and, therefore, a higher signal to noise ratio. Moreover, PMMA is a photo-elastic material, and nonpolarized light neutralizes photoelastic effects that could affect the intensity of the transmitted light.

Strain measurements. We use miniature Vishay 015RJ rosette strain gauges for local measurements of a 2D strain tensor. 19 such strain gages are mounted along and $\sim 3.5\,\text{mm}$ above the frictional interface, on one side of the upper block (Fig. 1a). All strain signals (57 channels) are amplified (gain ~ 400, $\sim 1\,\text{MHz}$ bandwidth) and simultaneously acquired to 14 bit accuracy by an ACQ132 digitizer (D-tAcq Solutions Ltd) which simultaneously acquires all strain signals at a 1 MHz rate. Acquisition is synchronized with the contact area measurements.

Dimensions of the strain gauges are presented in Extended Data Fig. 1b. The active size of each strain component is $0.34 \times 0.38\,\text{mm}$. The measured strain components, ε_1, ε_2, ε_3, are later converted to ε_{xy}, ε_{xx}, ε_{yy} by means of simple linear transformations:

$$\varepsilon_{yy} = \varepsilon_1$$
$$\varepsilon_{xy} = 1/2(\varepsilon_3 - \varepsilon_2) \qquad (3)$$
$$\varepsilon_{xx} = \varepsilon_3 + \varepsilon_2 - \varepsilon_1$$

Direct displacement, u_x, measurements:. Two Philtec D20 optical displacement sensors were used to monitor the local motion in the x direction, u_x, at different locations along the top block (Extended Data Fig. 1c, for clarity only one is shown). The original operation method of the Philtec sensor is based on measuring the reflectance of the transmitted light from a mirror target moving in a direction parallel to the light beam. As we need to measure displacement, u_x, perpendicular to the sensor's axis (Extended Data Fig. 1c, right), we used the sensor in a different way—making use of the fact that the sensor is, in essence, a reflectance sensor.

Thus, if a larger area of the light spot is incident on the reflective target, a larger signal is measured. As the target moves (in the x direction), different fractions of the spot area are reflected and the measured signal varies with u_x (Extended Data Fig. 1b, left). This signal is calibrated, and a ~ 0.1 μm resolution at an acquisition rate of 1 MHz is obtained. The sub-millimetre size of these sensors allows us to therefore obtain local measurements at extremely high precision and rapid rates.

Local material velocity, $\dot{u}_x$, measurements:. Local material velocity, $\dot{u}_x$, is determined by the numerical time derivative of the displacement, u_x, measured by the displacement sensor. Measurements of u_x, however, require delicate mounting and calibration of the displacement sensor. It is, therefore, extremely difficult to mount several sensors along the interface. In what follows, a more easily accessible technique is presented.

If the rupture propagation velocity, C_f, varies adiabatically, we can assume $u_x(x,t) = u_x(x - C_f t)$. As $\varepsilon_{xx} = \frac{\partial u_x}{\partial x}$, we can obtain the local material velocity via $\frac{\partial u_x}{\partial t} = -C_f \varepsilon_{xx}$ (for convenience, in the text we denote $\frac{\partial u_x}{\partial t}$ by $\dot{u}_x$). Therefore, the measured ε_{xx} combined with measurement of C_f can be used to measure the material velocities at each strain gauge site. As we measure ε_{xx} in 19 locations along the interface and C_f is extracted from the instantaneous location of the rupture tip (measurements of $A(x,t)$), this technique enables a relatively dense measurement of $\dot{u}_x$ along the interface without any additional preparations.

This technique was checked explicitly in several experiments, when displacement sensors were mounted slightly below one of the strain gauges and simultaneously measured. Extended Data Fig. 2 shows typical experiments where this technique is compared with direct displacement measurements. As the figure shows, the agreement between the two techniques is often within our measurement error.

Converting temporal to spatial measurements. The distance between adjacent strain gauges ($\sim 1\,\text{cm}$) is too large to provide good resolution of the spatial variation of the rapidly propagating fronts (Fig. 2b). We implement a high temporal resolution (1 μs) to overcome this difficulty. We assume that locally, the rupture is quasi-steady, $\varepsilon_{ij}(x,t) = \varepsilon_{ij}(x - C_f)$. Therefore, temporal measurements of $\varepsilon_{ij}(x = x_0, t)$ (x_0 is the position of the strain gauge) and C_f, together with the transformation $t \to -t C_f$, allow us to dramatically increase our spatial resolution. Extended Data Fig. 2 demonstrates typical examples where this quasi-steady assumption was verified. We compensated for slow spatial variations of $C_f(x)$ by using $\varepsilon_{ij}(x,t) = \varepsilon_{ij}(x - \int C_f dt)$ instead of $\varepsilon_{ij}(x,t) = \varepsilon_{ij}(x - C_f)$, where $C_f(t)$ was obtained from $A(x,t)$ measurements.

Comparing LEFM to measured strains. Strain gauge finite dimensions. Both the finite dimensions (Extended Data Fig. 1b) of the strain gauges and the temporal resolution of the acquisition system should be taken into account for proper interpretation of the measured strain signals of rapidly propagating ruptures. In order to accurately compare theory and measurements we convert the strain components ε_{xy}, ε_{xx}, ε_{yy}, predicted by LEFM, to ε_1, ε_2, ε_3 (for orientation of the measured strain components, see Extended Data Fig. 1b) by the inverse transformation of equation (3). After ε_1, ε_2, ε_3 were spatially averaged in accordance with both the geometry of the strain gauge components and the temporal differences due to the finite distances between the components, theoretical values corresponding to the measured ε_{ij} were obtained. These were the basis of the comparisons performed in Figs 2 and 3.

Boundary conditions. The universal LEFM solution is given[10] for both plane stress ($\sigma_{zz} = 0$) and plane strain ($\varepsilon_{zz} = 0$) boundary conditions. Plane stress boundary conditions are considered to be relevant when a thin plate with traction-free faces is considered. This assumption should be violated close to the frictional interface where the material is pinned—and therefore not allowed to expand freely in z direction. Moreover, when short wavelength (compared to the width of the sample) signals are considered, plane strain boundary conditions are generally more appropriate. This might be relevant for rapid ruptures.

In our experiments we expect that some mixture of the two boundary conditions might take place. Extended Data Fig. 3 demonstrates that while both solutions have similar characteristic features some differences are apparent; measurements of ε_{xx} are slightly better described by the plane stress solution, whereas measurements of ε_{yy} are significantly better described by plane strain.

These considerations, however, are beyond the scope of the current work and in the main text we compare our measurements with the solution dictated by plane strain boundary conditions alone.

LEFM coupled to simple cohesive zone model. The universal square-root singularity, predicted by LEFM, must be regularized by dissipative processes taking place in the vicinity of the crack tip. Therefore, it should be interpreted as 'intermediate asymptotics'; the universal functional form is expected to describe the elastic fields at distances far from the interface weakening region, X_c, but still small compared to other dimensions of the system[11]. This assumption is known as 'small scale yielding'. For high C_f, X_c is sufficiently small to have a clear separation of

scales. In the slow rupture regime the measurements were performed at a height $h = 3.5$ mm above the interface, which is a scale that is comparable to X_c (~ 2.5 mm at low velocities). The measured strains, however, are surprisingly well-described by the theory. This observation is perfectly compatible with simple cohesive zone models[11,22], as we demonstrate in Extended Data Fig. 4.

The effect of higher order terms. The complete LEFM stress field consists of a singular, $r^{-1/2}$, term together with additional (non-universal) terms of the form $r^{1/2}$, $r^{3/2}$, and so on, which vanish at the tip but may be significant at distances away from the crack tip.

Following the general solution procedure described in refs 10 or 22 we can derive the full angular dependence of these contributions to the stress field:

$$\sigma_{xy}(r,\theta) = C_n(2\pi r)^{\frac{n}{2}}\frac{1}{D(v)}\left(4\alpha_d\alpha_s\gamma_d^2\cos\left(\frac{n\theta_d}{2}\right) - (1+\alpha_s^2)^2\gamma_s^2\cos\left(\frac{n\theta_s}{2}\right)\right)$$

$$\sigma_{yy}(r,\theta) = -C_n(2\pi r)^{\frac{n}{2}}\frac{2\alpha_s(1+\alpha_s^2)}{D(v)}\left(\gamma_d^{\frac{n}{2}}\sin\left(\frac{n\theta_d}{2}\right) - \gamma_s^{\frac{n}{2}}\sin\left(\frac{n\theta_s}{2}\right)\right)$$

where the functions $\alpha_s,\alpha_d,\gamma_s,\gamma_d,\theta_s,\theta_d,D$ are defined in ref. 10, $n = -1,1,3,5...$ (odd terms are considered here) and C_n are numerical constants. For $n = -1$ we reconstruct the universal form with $C_{-1} = K_{II}$. Generally, for $n > -1$ the constants C_n are not universal and cannot be easily determined.

We now demonstrate that these terms will not resolve the discrepancy, observed for high C_f, in $\Delta\varepsilon_{xy}$ between the singular LEFM term and the measured signal, as presented in Fig. 3b, bottom. For simplicity, we consider the contribution of the terms $n = 1,3$. We attempt to resolve the discrepancies in $\Delta\varepsilon_{xy}$ in the range $0 < x - x_{tip}$ by varying C_1 and C_3 under the constraint that we can still reasonably describe $\Delta\varepsilon_{xx}$ and $\Delta\varepsilon_{yy}$. As Extended Data Fig. 5 demonstrates, these terms are insufficient to resolve the $\Delta\varepsilon_{xy}$ discrepancies in the range $0 < x - x_{tip} < 25$ mm while still demanding consistency with the measured data for $|x - x_{tip}| > 25$ mm. Assuming that the next terms ($n > 3$) will dominate at even larger distance, we conclude that, within this framework, the observed discrepancy is not resolved.

Estimating cohesive zone properties. Our measured values of Γ and X_c can provide rough estimates of cohesive zone properties. Let us assume a slip weakening model[11,12] in which the stress singularity predicted by LEFM is regularized by a peak shear stress, τ_p, that degrades to a residual strength, τ_r, over a slip distance, d_c. For simplicity, the weakening within the cohesive zone is assumed to be linear. It is then found that for slow ruptures, $X_c^0 = \frac{9\pi}{32} \times \frac{K_{II}^2}{(\tau_p - \tau_r)^2}$, where K_{II} is calculated from $\Gamma = [(1 - v^2)/E]K_{II}^2$

(ref. 11). Using the values Γ and X_c^0 from the text and the dynamic values of the Poisson ratio and Young's modulus, we find $\tau_p - \tau_r \approx 1.6 \pm 0.4$ MPa. For the conditions applied in the current experiments, $\tau_r \approx 3.7 \pm 0.4$ MPa. This leads to an estimation of $\tau_p \approx 5.3 \pm 0.8$ MPa. The linear slip weakening model also estimates that $\Gamma = 1/2(\tau_p - \tau_r)d_c$. This yields $d_c \approx 1.4$ μm, which is consistent with the asperity size of our rough interface.

Using this value of d_c, we can estimate, using simple scaling arguments[27,34], the maximal slip velocity $v_{max} \approx C_f d_c/X_c$. Thus, the contraction of X_c in Fig. 4c indicates strong growth of v_{max}, which was shown in recent numerical simulations[34]. Using $\dot{u}_x = -C_f\varepsilon_{xx}$ we obtain, for example in Fig. 2b at $C_f = 0.96C_R$, a maximal value of $\dot{u}_x \approx 0.3$ m s^{-1} measured 3.5 mm above the interface. At the interface, for the same C_f, the model then predicts 7 times larger velocity ($\dot{u}_x \approx 2$ m s^{-1}). Following this procedure, our maximal measured velocity of ~ 1 m s^{-1} (Fig. 3a) corresponds to at least $\dot{u}_x \approx 10$ m s^{-1} at the interface.

This discussion suggests that caution should be used when interpreting measurements at a finite distance from the interface as representative of processes at the interface.

Considering the value of Γ. For our experimental conditions, A is approximately 0.5% of the nominal contact area[4]. For different applied normal stresses this value will change. In addition, A is typically reduced (Fig. 4a) by about 20% during the rupture process. As a result, the value of $\Gamma \approx 1.1$ J m^{-2} results from a reduction of approximately 0.1% of the nominal fracture area. Γ therefore corresponds to a bulk fracture energy (a 100% reduction of the nominal fracture energy) of about $\Gamma_{Bulk} \approx 1,100$ J m^{-2}. This value is close to the measured value of Γ_{Bulk} for mode I fracture experiments in PMMA[35] and had been previously estimated for frictional dissipation using a thermal argument[2].

31. Read, B. E. & Duncan, J. C. Measurement of dynamic properties of polymeric glasses for different modes of deformation. *Polym. Test.* **2**, 135–150 (1981).
32. Rubinstein, S. M., Shay, M., Cohen, G. & Fineberg, J. Crack-like processes governing the onset of frictional slip. *Int. J. Fract.* **140**, 201–212 (2006).
33. Rubinstein, S. M., Cohen, G. & Fineberg, J. Visualizing stick-slip: experimental observations of processes governing the nucleation of frictional sliding. *J. Phys. D* **42**, 214016 (2009).
34. Gabriel, A. A., Ampuero, J. P., Dalguer, L. A. & Mai, P. M. Source properties of dynamic rupture pulses with off-fault plasticity. *J. Geophys. Res.* **118**, 4117–4126 (2013).
35. Sharon, E., Gross, S. P. & Fineberg, J. Energy dissipation in dynamic fracture. *Phys. Rev. Lett.* **76**, 2117–2120 (1996).
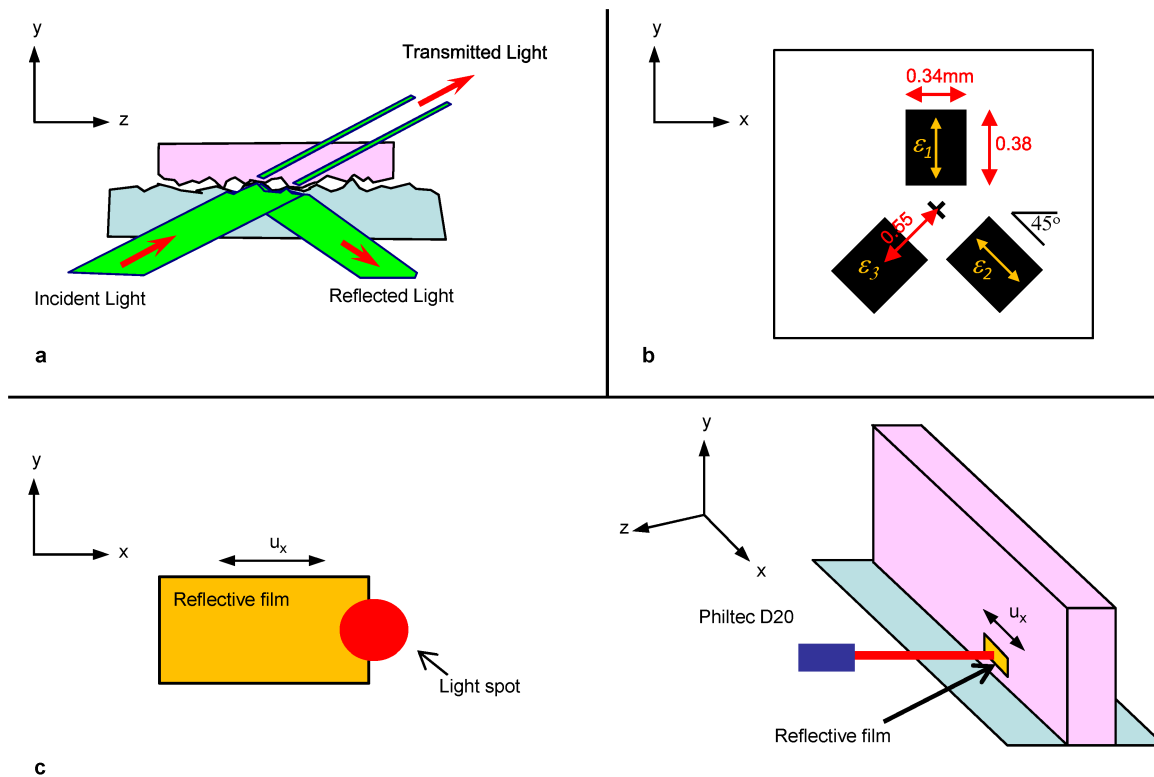
Extended Data Figure 1 | Experimental techniques. a, A method based on total internal reflection measures instantaneous changes in the real contact area, $A(x,t)$, along the entire interface. A sheet of light incident on the frictional interface is totally reflected everywhere except at contact points. Top block, pink; bottom block, blue. **b,** Geometry and dimensions (in mm) of a single rosette strain gauge. The black rectangles represent the active area of the measuring components, ε_1, ε_2 and ε_3. Yellow arrows represent the direction of the measured strains. **c,** By placing a reflective displacement sensor at the edge of a reflecting film (left), the change in the reflected signal is a monotonic function of the displacement of the film. The reflecting area was calibrated to obtain high resolution measurements of the motion of the strip edge in the x direction (right). **a–c,** Measurements described above were acquired continuously. A sensitive acoustic sensor, mounted on the top block, triggered storage of all data bracketing every slip event.

a

b
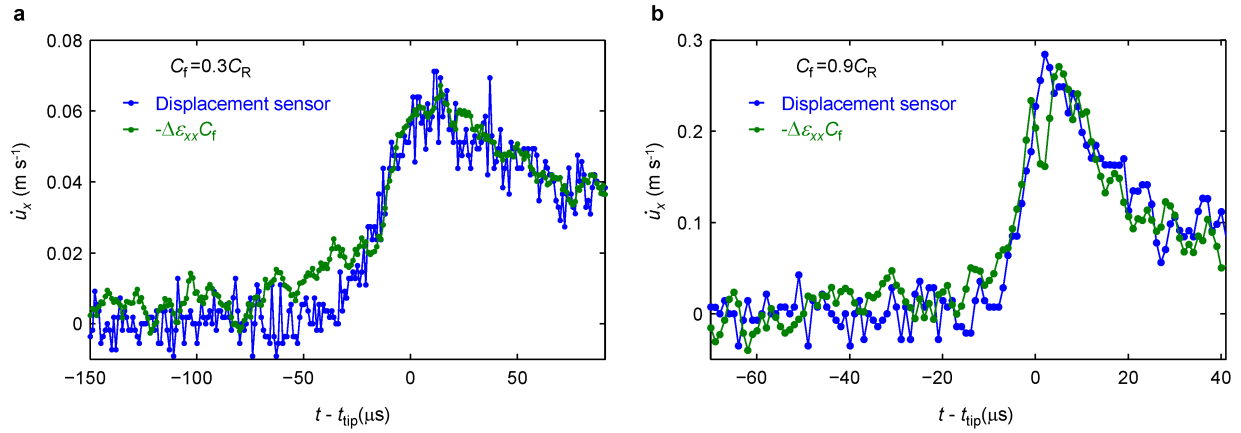
Extended Data Figure 2 | Comparing different techniques for measuring $\dot{u}_x$. In several experiments, direct displacement measurements were performed slightly below the strain gauge. The numerical time derivative of the corresponding signal is presented in blue. We reconstruct $\dot{u}_x$ by an alternative method (green) that is based on measuring C_f, $\Delta\varepsilon_{xx}$ and the assumptions presented in the text. **a, b**, Comparisons of $\dot{u}_x$ by using both methods for two typical examples at $C_f = 0.3C_R$ (**a**) and $C_f = 0.9C_R$ (**b**) show good agreement between the measurements. x axes are the times relative to the time, t_{tip}, when the rupture fronts passed each measurement location.
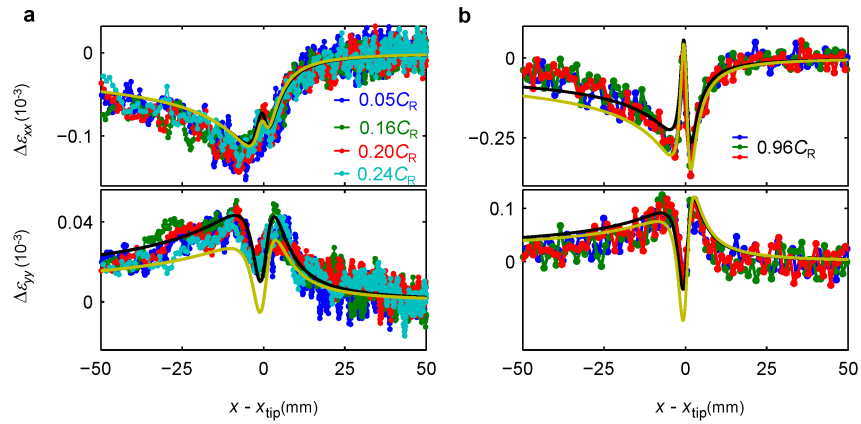
Extended Data Figure 3 | LEFM solution for plane strain and plane stress boundary conditions. a, b, Strain measurements of slow (**a**) and rapid (**b**) ruptures as presented in Fig. 2b. The top (bottom) panels are the strain components ε_{xx} (ε_{yy}) relative to their initial values immediately prior to rupture. The data presented are coloured as noted in the keys in the upper panel of **a** and

b. The solution for plane strain boundary conditions is shown in black. The solution for plane stress boundary conditions is shown in yellow. We see that plane strain conditions, as might be enforced by frictional pinning at the interface, provide a better fit to the data.
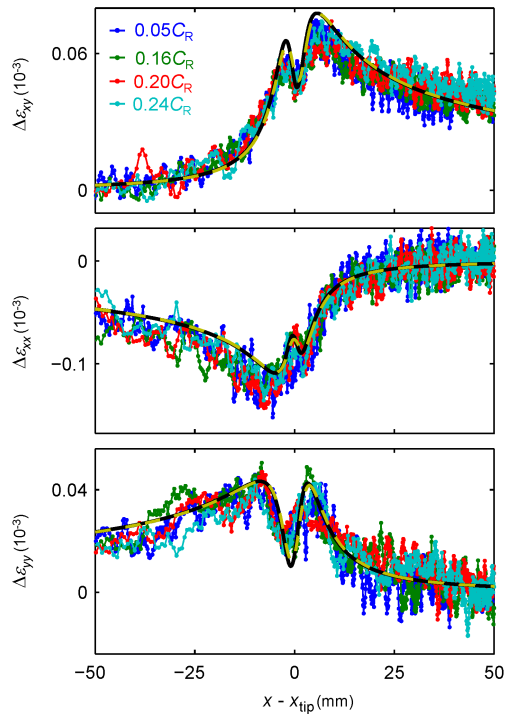
Extended Data Figure 4 | Comparing LEFM to linear cohesive zone model predictions. Strain measurements of a slow rupture as presented in Fig. 2a. Top, the strain component ε_{xy}, relative to the residual strain after the rupture passage. The centre (bottom) panels are the strain components ε_{xx} (ε_{yy}) relative to their initial values immediately prior to rupture. The data presented are coloured as noted in the key in the upper panel. Black solid line, the universal LEFM solution at 3.5 mm above the interface. Yellow dashed line, prediction of LEFM coupled to a linear slip weakening model[11,22] for $X_c = 2.5$ mm and using the same value of Γ as used in the LEFM solution 3.5 mm above the interface. In the slow rupture regime, for $h/X_c \approx 1$ (h is distance of the strain gauge above the interface) linear slip weakening model is indistinguishable from the singular LEFM solution.
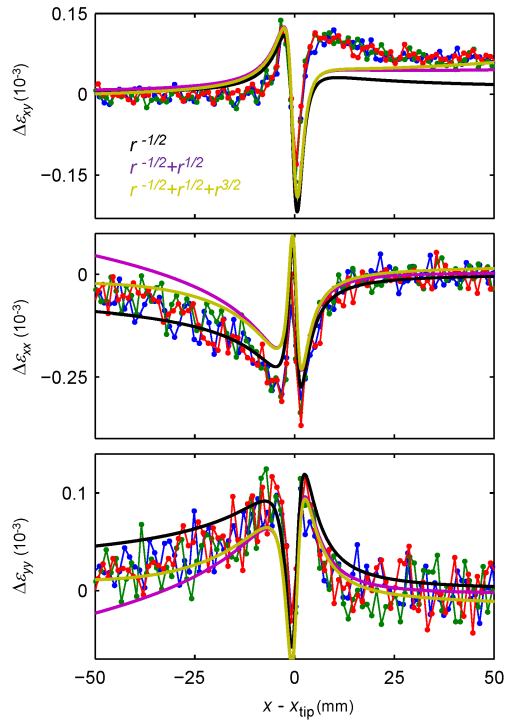
Extended Data Figure 5 | Contributions of higher-order terms to LEFM.
Strain measurements of a rapid rupture as presented in Fig. 2b. Top, the strain component ε_{xy}, relative to the residual strain after the rupture passage. The centre (bottom) panels are the strain components ε_{xx} (ε_{yy}) relative to their initial values immediately prior to rupture. The data presented are for three different measurements in which $C_f = 0.96C_R$. The key in the upper panel denotes the terms that were considered for each coloured line. No value of the $r^{1/2}$ (C_1) and $r^{3/2}$ (C_3) coefficients could both resolve the discrepancy in $\Delta\varepsilon_{xy}$ and reasonably fit $\Delta\varepsilon_{yy}$ and $\Delta\varepsilon_{xx}$.